American Mineralogist, Volume 81, pages 940–951, 1996

$^{40}Ar^*$ diffusion in Fe-rich biotite

MARTY GROVE AND T. MARK HARRISON

Department of Earth and Space Sciences and IGPP, University of California, Los Angeles, California 90024, U.S.A.

ABSTRACT

Hydrothermal bulk-loss experiments employing radiogenic Ar ($^{40}Ar^*$) were performed to determine whether $^{40}Ar^*$ diffusivity in biotite increases with Fe content. Diffusion laws determined for intermediate and Fe-rich biotite assuming single-domain diffusion (infinite-cylinder geometry) are remarkably similar: Fe-mica biotite ($X_{annite} = 0.71$) $D = 0.40^{+0.96}_{-0.28}\exp[-(50500 \pm 2.2)/RT]$ and Cooma biotite ($X_{annite} = 0.54$) $D = 0.075^{+0.049}_{-0.021}\exp[-(47100 \pm 1.5)/RT]$. The nearly identical results for Fe-mica biotite and Cooma biotite and their similarity to those from previous studies indicate that most biotite grains of intermediate composition possess comparable $^{40}Ar^*$ diffusion properties. Because limited grain breakage and volumetrically minor recrystallization is unavoidable during hydrothermal heating in bulk diffusion experiments, these diffusion laws necessarily provide upper limits to $^{40}Ar^*$ loss by intercrystalline diffusion. The measured rates of $^{40}Ar^*$ loss from biotite agree reasonably well with expectations based on single-domain volume diffusion using infinite-cylinder geometry when experimental uncertainties are taken into account. However, lack of information regarding $^{40}Ar^*$ gradients within the hydrothermally treated mica prevents us from precluding more complex diffusion mechanisms involving high diffusivity pathways. In this paper we consider the significance of bulk-loss $^{40}Ar^*$ diffusion experiments and discuss how diffusion parameters determined in the laboratory may be applied to thermochronology provided suitable constraints are available.

INTRODUCTION

The ability to constrain temperature-time histories of rocks is of paramount importance for reconstruction of the evolution of the Earth's crust. Thermochronologic use of $^{40}Ar/^{39}Ar$ data for biotite or other phases requires evidence that radiogenic ^{40}Ar ($^{40}Ar^*$) loss in nature occurs by a quantifiable diffusive process and availability of appropriate diffusion parameters (McDougall and Harrison 1988). While field experiments relying upon the thermal effects of intrusions (e.g., Westcott 1966; Hanson and Gast 1967) unarguably represent the most direct approach for understanding the rates and processes of $^{40}Ar^*$ loss in minerals under crustal conditions, difficulties inherent in determining thermal histories of crustal rocks renders field calibration of diffusion laws problematic. Therefore, although extrapolation of diffusion parameters measured at higher temperatures and shorter time scales than those relevant to $^{40}Ar^*$ loss from minerals in nature is not without risk (e.g., Villa and Puxeddu 1994), the large uncertainties associated with field calibration emphasize the need for laboratory studies.

Because Ar has extremely low solubility in silicate minerals (Ozima and Podosek 1983), Ar diffusion experiments invariably employ natural $^{40}Ar^*$ as the diffusant. Hydrothermal experiments are required to study $^{40}Ar^*$ retentivity in biotite because of biotite's tendency to decompose when heated in atmosphere or in vacuo (Brandt et al. 1967; Vedder and Wilkins 1969; Sanz et al. 1983). Hydrothermal $^{40}Ar^*$ diffusion studies (Giletti 1974; Norwood 1974; Harrison et al. 1985; Hess et al. 1987; Onstott et al. 1991) of biotite samples of known composition are indicated in Figure 1. In this paper we present results from hydrothermal $^{40}Ar^*$ bulk-loss experiments performed with Fe-rich biotite (Fe-mica biotite; Govindaradu 1979; Table 1; Fig. 1). Previous $^{40}Ar^*$ diffusion studies (Norwood 1974; Harrison et al. 1985) have predicted that Fe-rich biotite was significantly less retentive of $^{40}Ar^*$ than intermediate $Fe^{2+}/(Mg + Fe^{2+})$ compositions. To compare directly the $^{40}Ar^*$ retentivity of Fe-rich biotite and that of biotite of intermediate composition, additional experiments using identical experimental techniques were performed on Cooma biotite; (Harrison et al. 1985; Table 1).

EXPERIMENTAL DESIGN

Diffusion coefficients were calculated from the bulk loss of $^{40}Ar^*$ from sized aggregates of biotite hydrothermally heated at constant temperature (e.g., Giletti 1974). This simple approach circumvents difficulties related to obtaining Ar measurements with micrometer-scale resolution and has produced results comparable to those of depth profiling (e.g., Kelley et al. 1994a) in orthoclase (Foland 1974). Fractional losses (f) were calculated according to

0003–004X/96/0708–0940$05.00

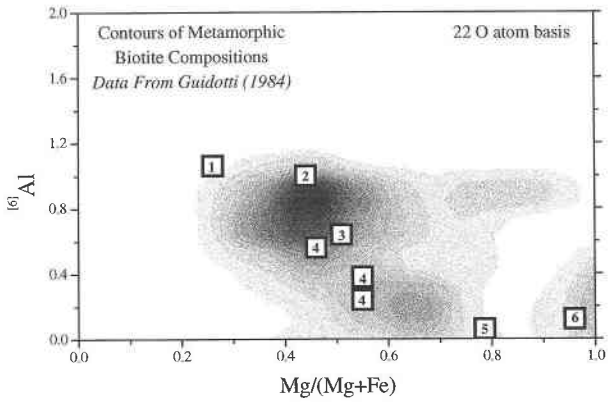

FIGURE 1. Contour plot of compositions of biotite from a wide spectrum of metamorphic rocks from subamphibolite to granulite facies; plot is based on data from Guidotti (1984). The black area indicates the region of the plot in which >5% of the analyses occur. Note the predominance of biotite of intermediate composition. Labeled squares represent compositions of biotite examined in hydrothermal $^{40}Ar^*$ studies: (1) Fe-mica biotite (this study), (2) Cooma biotite (Harrison et al. 1985), (3) intermediate biotite of Hess et al. (1987), (4) various biotite grains examined by Norwood (1974), (5) Benson Mines biotite (Onstott et al. 1991), and (6) F-rich phlogopite examined by Giletti (1974). Note that new electron microprobe analyses obtained for the biotite of Norwood (1974) are tabulated in Appendix Table 1.

$$f = \frac{{}^{40}Ar^*_u - {}^{40}Ar^*_h}{{}^{40}Ar^*_u} = \frac{\left(\frac{{}^{40}Ar^*}{{}^{39}Ar}\right)_u J_u - \left(\frac{{}^{40}Ar^*}{{}^{39}Ar}\right)_h J_h}{\left(\frac{{}^{40}Ar^*}{{}^{39}Ar}\right) J_u} \quad (1)$$

where u and h denote untreated and hydrothermally annealed biotite, and J is an experimentally determined constant characterizing production of ^{39}Ar from ^{39}K during neutron irradiation (McDougall and Harrison 1988). Use of Equation 1 assumes $^{40}Ar^*$ concentration within the grains is initially homogeneous and that external $^{40}Ar^*$ concentrations are maintained at zero (Crank 1975). The latter is guaranteed by an infinite reservoir of atmospheric Ar. Measurements of ^{36}Ar ($^{40}Ar/^{36}Ar_{ATM} = 295.5$) provided the basis for correcting for atmospheric ^{40}Ar incorporated into the grains during hydrothermal treatment. Following earlier studies (e.g., Giletti 1974), diffusion coefficients (D) were calculated with the assumption that $^{40}Ar^*$ loss during hydrothermal treatment occurs by single-domain, intracrystalline diffusion, with bulk $^{40}Ar^*$ transport normal to the c axis (infinite-cylinder geometry). The compatibility of the systematics of $^{40}Ar^*$ loss with these assumptions can be evaluated by comparing the measured values of f with those predicted by the model in plots of f vs. t/a^2 or equivalent representations (Crank 1975). Diffusivities were calculated using the approximate solution for the infinite cylinder of Reichenberg (1953):

$$\left(\frac{Dt}{a^2}\right) = \frac{4}{\pi}\left(1 - \sqrt{1 - \frac{\pi}{4}f}\right)^2 \quad (2)$$

TABLE 1. Biotite compositions

	Cooma* biotite	Fe-mica** biotite
Si	2.69	2.72
[4]Al	1.31	1.28
[6]Al	0.50	0.53
Ti	0.15	0.15
Fe^{3+}	0.07	0.27
Fe^{2+}	1.19	1.27
Mn	0.02	0.02
Mg	0.98	0.54
K	0.94	0.91
Na	0.02	0.04
Total Cations	7.87	7.73
OH	1.77	1.59
F†	0.12	0.40
Cl†	0.11	0.01

* XRF analysis and wet-chemical analysis (Tetley 1978).
** Wet-chemical analyses reported by Govindaradu (1979).
† F and Cl from electron probe analysis; OH by difference.

where t and a represent the heating duration and measured radii of the grain, respectively. Neglecting additional terms causes an error of <0.10 in natural log units for values of $Dt/a^2 < 0.05$. Activation energies (E_a) and frequency factors (D_0) were calculated in the conventional manner from the slope ($-E_a/R$) and ordinate (ln D_0) of an Arrhenius plot of the experimental results (ln D vs. inverse absolute temperature).

CHARACTERIZATION OF STARTING MATERIALS

The compositions of both Fe-mica and Cooma biotite were determined by wet-chemical methods and X-ray diffraction (XRD) (Table 1). Cell dimensions determined by R.E. Jones (UCLA) using XRD are $a = 5.335$, $b = 9.246$, $c = 10.190$ Å, $\beta = 100.24°$ for Fe-mica, and $a = 5.341$, $b = 9.237$, $c = 10.233$ Å, $\beta = 100.02°$ for Cooma biotite. Spot analysis by electron microprobe indicated homogeneous major element compositions. Both optical and backscattered electron imaging showed no detectable chlorite in either sample (see also analysis performed by Tetley 1978). This is also supported by high K_2O contents (Table 1) and the absence of basal reflections from chlorite in X-ray diffraction patterns. These observations do not preclude the presence of trace, nanometer-scale chlorite intergrowths (e.g., Hess et al. 1987; Onstott et al. 1991).

Distribution of $^{40}Ar^*$

Calculation of model diffusion coefficients requires homogeneously distributed $^{40}Ar^*$ in the host. Uniform $^{40}Ar^*$ concentrations are expected for Fe-mica because it is derived from a high-level intrusion (Roubault et al. 1968) that is likely to have cooled rapidly. Although the Cooma plutonic complex originated from somewhat deeper levels (~3 kbar; Vernon 1988), cooling at approximately 20 °C/Ma through its closure interval for Ar retention minimizes the potential for significant $^{40}Ar^*$ gradients (Tetley 1978). The $^{40}Ar/^{39}Ar$ step-heating experiments have yielded uniform age spectra for both Cooma biotite (Tetley 1978) and Fe-mica (Harrison, unpublished data). Unfortunately, these results do not require the absence of internal $^{40}Ar^*$ gradients because structural decomposition

TABLE 2. Cooma and Fe-mica biotite grain-size dimensions

Mesh size*	Length ⊥ (001) (μm)**	Width ⊥ (001) (μm)**	Effective radius (μm)†	Length/width
		Cooma biotite		
100–120	318 ± 65	202 ± 20	128 ± 13	1.6 ± 0.4
120–140	294 ± 71	166 ± 20	113 ± 13	1.8 ± 0.5
140–170	247 ± 58	134 ± 10	96 ± 10	1.8 ± 0.5
		Fe-mica biotite		
60–80	488 ± 99	305 ± 41	191 ± 23	1.6 ± 0.5
80–100	398 ± 84	241 ± 28	154 ± 17	1.7 ± 0.5
100–120	313 ± 72	203 ± 19	125 ± 14	1.6 ± 0.4
120–140	289 ± 82	168 ± 22	109 ± 15	1.8 ± 0.6
140–170	248 ± 73	141 ± 16	92 ± 13	1.8 ± 0.6
170–200	188 ± 45	113 ± 12	72 ± 9	1.7 ± 0.3
200–230	143 ± 53	88 ± 11	56 ± 10	1.6 ± 0.3

* Units are division per inch.
** Results of 100 measurements per size fraction.
† Effective radii (a) calculated from measured flake dimensions by $a = \sqrt{lw}/2$.

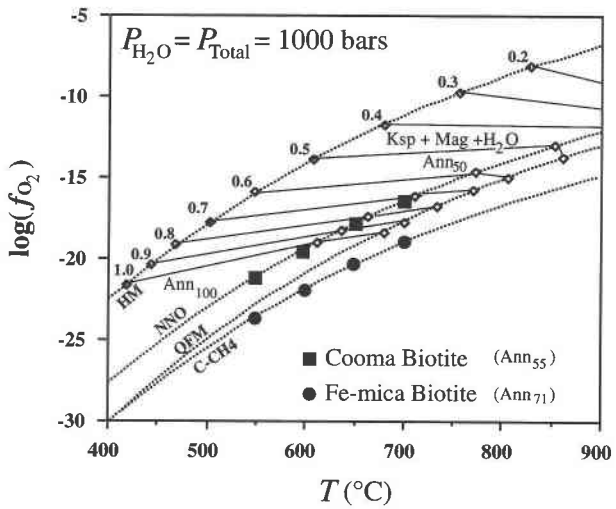

FIGURE 2. T-f_{O_2} stability relations of ferromagnesian biotite. Solid lines represent isopleths for annite + O_2 = magnetite + potassium feldspar + H_2O (values represent annite content of biotite). Phase relations are calculated for H_2O pressure of 1000 bars using data of Wones and Eugster (1965). Buffers shown by the dotted lines are hematite + magnetite (HM), Ni + NiO (NNO), quartz + fayalite + magnetite (QFM), and graphite + methane (C-CH_4). The solid squares and circles represent the experimental conditions for Cooma biotite and Fe-mica, respectively.

of biotite by dehydroxylation and basal delamination during in vacuo heating obscures $^{40}Ar^*$ gradients by homogenizing them (Hansen et al. 1975; Gaber et al. 1988). Both Fe-rich mica and Cooma biotite indicate homogeneous $^{40}Ar^*$ concentrations when sampled in bulk (~5 mg) aggregates. Harrison et al. (1985) reported a $^{40}Ar^*$ concentration of $6.001 \pm 0.009 \times 10^{-9}$ mol/g for three replicate analyses of Cooma biotite. Fe-mica ($^{40}Ar^* = 4.384 \times 10^{-9}$ mol/g; Govindaradu 1979) has been used in the UCLA $^{40}Ar/^{39}Ar$ facility for over 6 yr as a concentration standard for $^{40}Ar^*$. The $^{40}Ar^*/^{39}Ar$ ratios of aliquots of both coarse- and fine-size fractions of Fe-mica can be reproduced with the same precision (≤0.6%).

Sizing

Mica grains were sorted by dry and then wet sieving into seven size fractions between 80 and 230 mesh. Most grains possessed smooth basal cleavages with essentially vertical margins as measured from the basal cleavage. Long and short dimensions of cleavage faces were measured for at least 100 grains from each size fraction (Table 2). Diameter-to-flake thickness ratios estimated from known K_2O contents and ^{39}Ar yields obtained by fusing measured grains with an Ar ion laser were typically 25:1, in agreement with less precise optical determinations. Grain radii were estimated by calculating the area of the ellipse defined by the long and short dimensions of cleavage faces and then finding the radius of the equivalent area cylinder (Harrison et al. 1985). An alternative approach used by Giletti (1974) and Norwood (1974) yields a radius that is 12.8% larger and diffusion coefficients that are 20% smaller (~0.24 natural log units on an Arrhenius plot). This discrepancy is comparable to the experimental uncertainty in the measurement.

HYDROTHERMAL TREATMENT

Sized, 25 mg aliquots of biotite were sealed in either gold or $Ag_{70}Pd_{30}$ capsules with 1 mg pure water. Isothermal, isobaric heating was performed within externally heated, cold-seal pressure vessels under conditions indicated by previous experimental studies to be within their respective P-T-f_{O_2} stability fields (Fig. 2; see Wones and Eugster 1965; Rutherford 1973). Experiments were conducted at 550–700 °C and 1000 bars (Table 3). In Fe-mica experiments, T and f_{O_2} conditions were maintained at values imposed by the graphite + methane buffer with the use of thin-walled, $Ag_{70}Pd_{30}$ capsules and methane equilibrated with powdered graphite and graphite filler rods as the pressure medium (Huebner 1971). In Cooma biotite experiments, sufficient time (15–100 d) was likely available to permit equilibration through the 0.25 mm thick gold capsule walls with the intrinsic f_{O_2} of the Stellite 25 pressure vessel and the stainless steel filler rod (approximately that of the Ni + NiO buffer; Huebner 1971). Temperature was regulated with proportional controllers using dual Chromel-Alumel thermocouples. Pressure was monitored with a Heise-Bourdon gauge. After equilibration, variations in these parameters were generally less than ±1 °C and ±5 bars. Temperature calibration performed using two thermocouples agreed with expected values for the melting points of pure NaCl and Al wire within 5 °C. All samples were quenched in compressed air and removed from the pressure vessel within 5–10 min of power shut off. Charges were discarded if weighing routines indicated leakage of H_2O.

Light microscope and SEM imaging of treated mica revealed both appreciable breakage of original grains as well as new biotite growth. In general, hydrothermally treated Fe-mica biotite tended to exhibit a higher per-

TABLE 3. Cooma and Fe-mica biotite experimental results

Expt.	T (°C)	t (d)	a (μm)	f	ln D
			Cooma biotite		
HCB-1	550	97.13	96 ± 10	0.102 ± 0.006	−31.88 ± 0.25
HCB-2	550	97.13	113 ± 13	0.074 ± 0.004	−31.70 ± 0.32
HCB-3	600	50.29	113 ± 13	0.159 ± 0.004	−29.49 ± 0.25
HCB-4	600	50.27	128 ± 13	0.111 ± 0.004	−29.98 ± 0.24
HCB-5	650	28.91	128 ± 13	0.181 ± 0.005	−28.42 ± 0.22
HCB-6	650	28.95	128 ± 13	0.180 ± 0.004	−28.43 ± 0.22
HCB-7	700	15.89	128 ± 13	0.241 ± 0.003	−27.22 ± 0.21
HCB-8	700	15.93	128 ± 13	0.233 ± 0.006	−27.30 ± 0.21
			Fe-mica biotite		
Fm-12	700	78.09	154 ± 17	0.584 ± 0.003	−26.49 ± 0.22
Fm-1	700	15.07	125 ± 14	0.307 ± 0.006	−26.70 ± 0.23
Fm-9	700	22.01	109 ± 15	0.250 ± 0.006	−27.79 ± 0.29
Fm-3	700	15.07	92 ± 13	0.349 ± 0.006	−27.04 ± 0.29
Fm-10	700	14.03	92 ± 13	0.302 ± 0.006	−27.28 ± 0.29
Fm-2	650	25.88	125 ± 14	0.191 ± 0.006	−28.25 ± 0.24
Fm-5	650	44.16	125 ± 14	0.216 ± 0.006	−28.52 ± 0.24
Fm-4	650	20.98	92 ± 13	0.185 ± 0.004	−28.71 ± 0.30
Fm-6	650	14.86	92 ± 13	0.121 ± 0.007	−29.24 ± 0.32
Fm-8	600	23.91	56 ± 10	0.216 ± 0.007	−29.51 ± 0.38
Fm-15	600	75.93	56 ± 10	0.290 ± 0.007	−30.04 ± 0.38
Fm-11	550	78.09	109 ± 15	0.0443 ± 0.0101	−32.60 ± 0.60
Fm-13	550	75.93	92 ± 13	0.0948 ± 0.0076	−31.38 ± 0.34
Fm-14	550	75.93	56 ± 10	0.117 ± 0.009	−31.93 ± 0.42
Fm-16	550	67.92	56 ± 10	0.106 ± 0.007	−32.03 ± 0.40
Fm-17	550	67.92	56 ± 10	0.135 ± 0.007	−31.54 ± 0.39

centage of new grain growth. XRD patterns obtained for all experiments revealed only biotite peaks. Ultrasonic treatment and wet sieving under acetone was performed to recover from the capsules grains with dimensions similar to those of the original starting material. Only the mica grains with dimensions corresponding to those of the original size fraction (approximately 60–90% of the treated grains) were used in further analysis. SEM imaging of these materials indicated that <5–10% of the surface of treated grains was covered by neoformed, 1–10 μm diameter hexagonal platelets after ultrasonic treatment (Fig. 3). Note that original broken grain boundaries are well preserved even after heating at 700 °C for 78 d (Fig. 3a). Close inspection reveals that micrometer-scale biotite overgrowths forming euhedral margins are common on broken grain edges (Fig. 3b). Recrystallization on this scale probably represents <1% of the mass of the original grain. For example, reprecipitation of biotite to cover 10% of the surface with 10 μm diameter (1 μm thick) grains corresponds to 0.40% recrystallization.

$^{40}Ar/^{39}Ar$ ANALYSIS

Hydrothermally treated Fe-mica and Cooma biotite were analyzed for $^{40}Ar^*$ loss using the $^{40}Ar/^{39}Ar$ technique. Hydrothermally treated mica grains interspersed with untreated biotite and Fish Canyon sanidine (FCT-1) were irradiated for 120 h in the L67 position of the Ford reactor (University of Michigan). These conditions yielded J factors of ~0.02 (Table 4) and necessitated a correction factor for K-derived ^{40}Ar of 0.025 (determined from measurements on K_2SO_4). Gas extracted from ~5 mg splits of mica wrapped in tin foil in a double-vacuum tantalum resistance furnace was purified with an S.A.E.S. GP-50 Zr-Al getter pump and analyzed with a Nuclide 4.5–60-RSS mass spectrometer operated in the Faraday mode [^{40}Ar sensitivity of 1.5×10^{-15} mol/mV; mass discrimination of 0.994 per amu; see Harrison and Fitz Gerald (1986) and McDougall and Harrison (1988) for additional experimental details]. In each analysis, samples were degassed in a crucible preheated to 350 °C for ~5 min to melt the enclosing tin foil. Although this gas was generally not analyzed, measurements performed for the first several samples detected background ^{39}Ar values and atmospheric $^{40}Ar/^{36}Ar$ ratios. After pretreatment at 350 °C, temperature was increased to 850 °C for ~5 min to stabilize the mica grains by allowing them to dehydroxylate (Vedder and Wilkins 1969) before fusing them for ~5 min at 1350 °C. Although, blank determinations following this procedure were $<10 \times 10^{-14}$ mol at m/e 40, $<2 \times 10^{-16}$ mol at m/e 39, and $<1 \times 10^{-16}$ mol at m/e 36, sporadically low-percent $^{40}Ar^*$ yields measured for all materials indicate somewhat higher degrees of atmospheric contamination.

RESULTS

Results of the $^{40}Ar/^{39}Ar$ analyses of untreated and hydrothermally annealed Fe-mica and Cooma biotite are presented in Table 4. Note that approximately 30% of the analyses were performed on untreated mica. Total fusion ages were calculated with J factors determined by assigning an age of 27.8 Ma to Fish Canyon sanidine (Cebula et al. 1986). The age uncertainties include a 0.5% analytical uncertainty in J. Weighted mean ages and standard errors calculated from separate aliquots of untreated biotite were 307.6 ± 0.4 Ma (eight analyses) and 398.1 ± 0.7 Ma (19 analyses) for Fe-mica biotite and Cooma

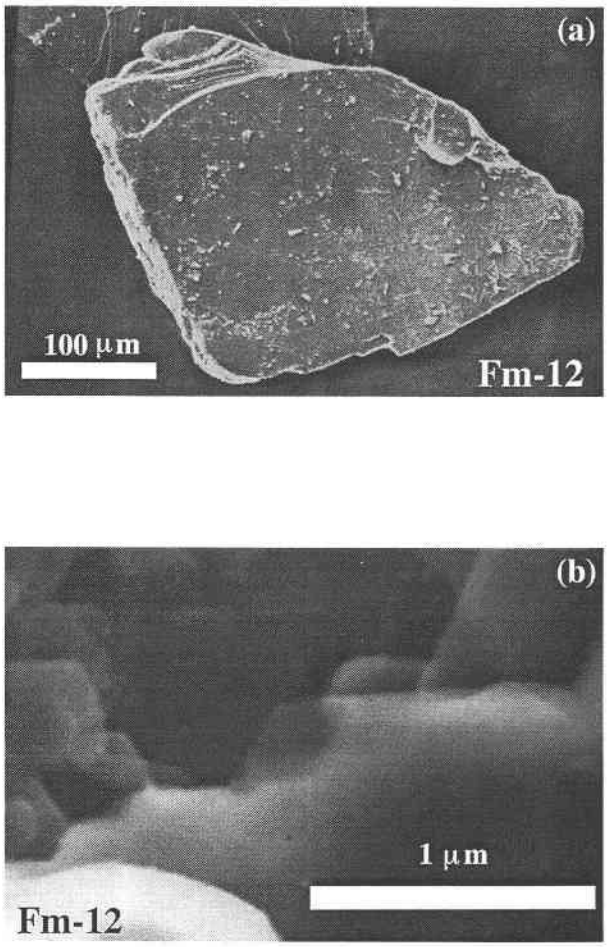

FIGURE 3. Representative SEM images of hydrothermally heated biotite. (a) Grain from experiment Fm-12, which was heated at 700 °C for 78 d (longest duration at 700 °C). Note that original fractured grain-boundary morphologies are well preserved. Note that the cleavage surface is affected by new mica growth of micrometer scale. As discussed in the text, recrystallization on this scale probably represents <1% of the mass of the original grain. (b) Close inspection of many broken surfaces reveals new euhedral biotite overgrowths of submicrometer scale. Note that an ~0.5 μm thick overgrowth covering the entire grain would correspond to only 1% recrystallization.

biotite, respectively. These results compare favorably with previous K-Ar age determinations of 307.3 ± 2.0 Ma for Fe-mica biotite (Harrison, unpublished data) and 398.8 ± 2.5 Ma for Cooma biotite (Tetley 1978). The homogeneous character of the starting material is indicated by <0.3% reproducibility in the total gas ages yielded by individual analyses (Table 4). The average uncertainty in total fusion age (excluding analytical uncertainty in J) is also 0.3%. Duplicate analyses were generally performed for treated mica from each experiment. Although only 40% of the total fusion ages calculated from duplicate analyses agreed to within 0.3%, nearly 80% reproduced to within 1%. Total fusion ages from hydrothermally treated Fe-mica biotite were more difficult to reproduce than those from treated Cooma biotite (Table 4).

Fractional loss (f) values for the hydrothermally treated mica calculated with Equation 1 are shown in Table 3. Most values of f were computed from the average of two replicate analyses from the same experiment. Propagation of errors associated with $^{40}Ar^*/^{39}Ar$ and J indicate that relative uncertainties in fractional loss values in the range $0.10 < f < 0.50$ are ~5% (on the order of ±0.01 units in fractional loss). The uncertainties in fractional loss for a given experiment appear to account for overall experimental reproducibility. For example, values of fractional loss determined for two sets of nearly identical experiments (HCB-5 and HCB-6, HCB-7 and HCB-8) agreed to within 0.4 and 3.5%, respectively (Table 3). For fractional loss values <0.10, relative uncertainties approach 25%.

Model diffusion coefficients (D) calculated with Equation 2 are also shown in Table 3. Uncertainties reported for D are typically ±0.3 natural log units and reflect ±1σ uncertainties in both fractional loss and estimated grain size (Table 3). Note that asymmetric uncertainties in ln D were rounded in Table 3. At a given temperature, experimental reproducibility (±0.5 natural log units) is nearly accounted for by experimental uncertainty at the ±2σ level. This scatter likely results from minor (<1%) recrystallization during hydrothermal treatment and from the presence of small grain fragments formed during initial experimental pressurization but not removed during subsequent ultrasonic cleaning and resizing.

Least-squares regression of the Arrhenius data for Fe-mica using a ±5 °C uncertainty in temperature yields 50.5 ± 2.2 kcal/mol and $0.40^{+0.96}_{-0.28}$ cm²/s (MSWD = 2.1) for E_a and D_0, respectively (Fig. 4a). Following the same procedure for Cooma biotite yields an E_a of 44.5 ± 2.5 kcal/mol and a D_0 of $0.015^{+0.022}_{-0.005}$ cm²/s (MSWD = 0.57). These values are within 1σ of those obtained by Harrison et al. (1985), who reported 47 ± 2.1 kcal/mol and $0.077^{+0.21}_{-0.06}$ cm²/s for E_a and D_0, respectively. Combining the data obtained for Cooma biotite in the two studies yields values of 47.1 ± 1.5 kcal/mol and $0.075^{+0.049}_{-0.021}$ cm²/s (MSWD = 1.25) for E_a and D_0, respectively. Considering the large experimental uncertainty, these values are essentially the same as those obtained for Fe-mica biotite. The higher degree of scatter exhibited by Fe-mica may reflect greater recrystallization and comminution of grains than was observed in experiments performed with Cooma biotite.

DISCUSSION

Significance of biotite bulk-loss $^{40}Ar^*$ diffusion experiments

Taking experimental uncertainty into account, loss of $^{40}Ar^*$ from biotite in the present experiments agrees reasonably well with expectations based on the single-domain diffusion model with infinite-cylinder geometry. This compatibility is illustrated in Figure 5. In this diagram, values of t/a^2 calculated from the measured grain size and heating duration are plotted against measured fractional loss. Also shown are single-domain solutions for the infinite cylinder at the indicated temperatures. As

TABLE 4. Cooma and Fe-mica biotite $^{40}Ar/^{39}Ar$ analytical results

Expt.	J factor	Weight (mg)	$^{39}Ar \times 10^{-12}$ mol	Equivalent % K_2O	% $^{40}Ar^*$	$^{40}Ar^*/^{39}Ar$	Apparent age (Ma)
			Cooma biotite				
HCB-1	0.02054	3.45	1.89	10.3	74.5	10.79	361.1 ± 2.2
HCB-2	0.02055	3.40	1.81	10.0	56.5	11.17	372.8 ± 2.1
HCB-2	0.02055	5.87	2.90	9.2	81.6	11.07	369.8 ± 1.8
HCB-3	0.02055	5.49	2.84	9.7	68.7	10.12	340.9 ± 1.7
HCB-3	0.02055	6.83	3.54	9.7	76.6	10.09	339.9 ± 1.7
HCB-4	0.02055	5.47	2.99	10.2	85.6	10.71	358.9 ± 1.7
HCB-4	0.02055	3.66	2.09	10.7	78.9	10.65	357.1 ± 1.7
HCB-5	0.02055	2.91	1.57	10.1	55.7	9.84	332.2 ± 1.6
HCB-6	0.02057	5.48	2.89	9.9	65.3	9.84	332.5 ± 2.0
HCB-6	0.02057	5.43	2.83	9.7	76.6	9.84	332.5 ± 1.6
HCB-7	0.02057	9.93	5.05	9.5	83.6	9.11	309.9 ± 1.6
HCB-7	0.02057	5.64	2.95	9.8	77.6	9.11	309.9 ± 1.7
HCB-8	0.02058	5.45	2.91	10.0	67.8	9.17	311.9 ± 1.7
HCB-8	0.02058	7.16	3.70	9.7	76.1	9.24	314.1 ± 1.6
Untreated	0.02054	3.87	2.02	9.8	91.3	12.01	397.8 ± 1.9
Untreated	0.02054	6.07	3.11	9.6	86.4	12.06	399.3 ± 1.9
Untreated	0.02054	6.49	3.41	9.8	91.8	12.02	398.1 ± 1.9
Untreated	0.02056	6.01	3.10	9.6	92.0	12.00	397.8 ± 1.9
Untreated	0.02056	6.98	3.56	9.5	84.8	11.98	397.2 ± 1.8
Untreated	0.02060	6.25	3.16	9.4	74.3	12.00	398.5 ± 1.8
Untreated	0.02060	10.10	4.91	9.1	86.8	11.96	397.3 ± 2.0
Untreated	0.02060	5.51	3.01	10.2	85.8	12.00	398.5 ± 2.0
			Fe-mica biotite				
Fm-1	0.02087	3.77	2.00	9.8	50.9	6.18	218.9 ± 1.4
Fm-1	0.02087	7.37	3.52	8.8	50.3	6.16	218.2 ± 1.2
Fm-2	0.02094	3.19	1.71	9.8	73.5	7.18	252.7 ± 1.3
Fm-2	0.02094	6.07	3.11	9.4	73.4	7.19	253.0 ± 1.2
Fm-3	0.02103	4.36	1.14	4.8	68.1	5.70	204.2 ± 1.2
Fm-3	0.02103	4.81	2.33	8.9	63.9	5.81	208.0 ± 1.2
Fm-4	0.02107	4.00	2.04	9.3	84.8	7.20	254.8 ± 1.4
Fm-4	0.02107	3.56	1.32	6.8	61.2	7.18	254.2 ± 1.5
Fm-5	0.02044	5.32	2.69	9.5	69.1	7.14	245.8 ± 1.2
Fm-5	0.02044	5.47	2.74	9.4	82.0	7.12	245.1 ± 1.2
Fm-6	0.02042	4.48	2.25	9.5	81.6	8.00	273.0 ± 1.4
Fm-6	0.02042	7.31	3.43	8.8	84.4	8.00	273.0 ± 1.4
Fm-8	0.02040	5.26	2.46	8.8	65.5	7.14	245.3 ± 1.3
Fm-9	0.02039	4.52	2.30	9.6	85.0	6.80	234.3 ± 1.1
Fm-9	0.02039	4.36	2.24	9.7	74.9	6.87	236.5 ± 1.5
Fm-10	0.02038	6.16	2.78	8.5	88.0	6.35	219.6 ± 1.1
Fm-10	0.02038	3.56	1.69	9.0	63.3	6.38	220.5 ± 1.2
Fm-11	0.02037	4.59	2.10	8.6	39.4	8.70	294.3 ± 1.6
Fm-11	0.02037	7.65	3.27	8.1	42.9	8.74	295.6 ± 2.3
Fm-12	0.02037	6.69	3.52	9.9	72.4	3.82	135.2 ± 0.7
Fm-12	0.02037	5.85	3.25	10.5	64.9	3.78	133.8 ± 0.7
Fm-13	0.02037	1.89	0.891	8.9	86.3	8.32	282.4 ± 1.6
Fm-13	0.02037	4.37	2.18	9.4	84.8	8.20	278.7 ± 1.4
Fm-14	0.02038	3.14	1.59	9.6	77.1	7.88	268.7 ± 1.4
Fm-14	0.02038	1.26	0.634	9.5	41.9	8.22	279.4 ± 2.3
Fm-15	0.02040	2.05	0.664	6.1	79.8	6.57	226.9 ± 1.4
Fm-15	0.02040	3.70	1.68	8.6	70.8	6.36	220.1 ± 1.4
Fm-16	0.02041	6.29	3.01	9.0	77.8	8.11	276.3 ± 1.3
Fm-16	0.02041	4.06	2.07	9.6	77.2	8.17	278.2 ± 1.4
Fm-17A	0.02042	5.00	2.49	9.4	69.7	7.81	267.0 ± 1.4
Fm-17A	0.02042	5.38	2.61	9.1	79.1	7.94	271.1 ± 1.4
Untreated	0.02046	5.85	2.97	9.5	96.6	9.18	310.5 ± 1.6
Untreated	0.02046	4.30	2.10	9.2	88.9	9.08	307.4 ± 1.5
Untreated	0.02046	2.83	1.21	8.0	67.4	9.07	307.1 ± 1.7
Untreated	0.02038	8.09	4.27	10.0	94.0	9.11	307.2 ± 1.5
Untreated	0.02038	2.65	1.29	9.2	93.5	9.23	311.0 ± 1.7
Untreated	0.02039	5.40	2.68	9.4	83.4	9.09	306.8 ± 1.7
Untreated	0.02039	3.24	1.58	9.2	63.3	9.13	308.0 ± 1.5
Untreated	0.02039	5.80	2.99	9.7	68.2	9.09	306.8 ± 1.5
Untreated	0.02044	4.3	2.12	9.3	78.0	9.11	308.1 ± 1.9
Untreated	0.02044	3.85	1.90	9.3	85.1	9.09	307.4 ± 1.5
Untreated	0.02044	2.62	1.35	9.7	77.8	9.07	306.8 ± 1.5
Untreated	0.02046	5.28	2.40	8.5	62.7	9.08	307.4 ± 1.7
Untreated	0.02046	7.20	3.55	9.3	90.8	9.12	308.7 ± 1.5
Untreated	0.02082	4.57	1.97	8.0	84.4	8.91	307.0 ± 1.7
Untreated	0.02082	5.89	2.88	9.0	89.7	8.93	307.6 ± 1.5
Untreated	0.02082	2.45	1.30	9.8	29.5	8.63	298.1 ± 2.6
Untreated	0.02114	7.13	3.61	9.2	86.2	8.75	306.2 ± 1.5
Untreated	0.02114	5.85	2.91	9.1	95.2	8.80	307.8 ± 1.6
Untreated	0.02114	7.45	3.41	8.3	72.5	8.80	307.8 ± 1.5

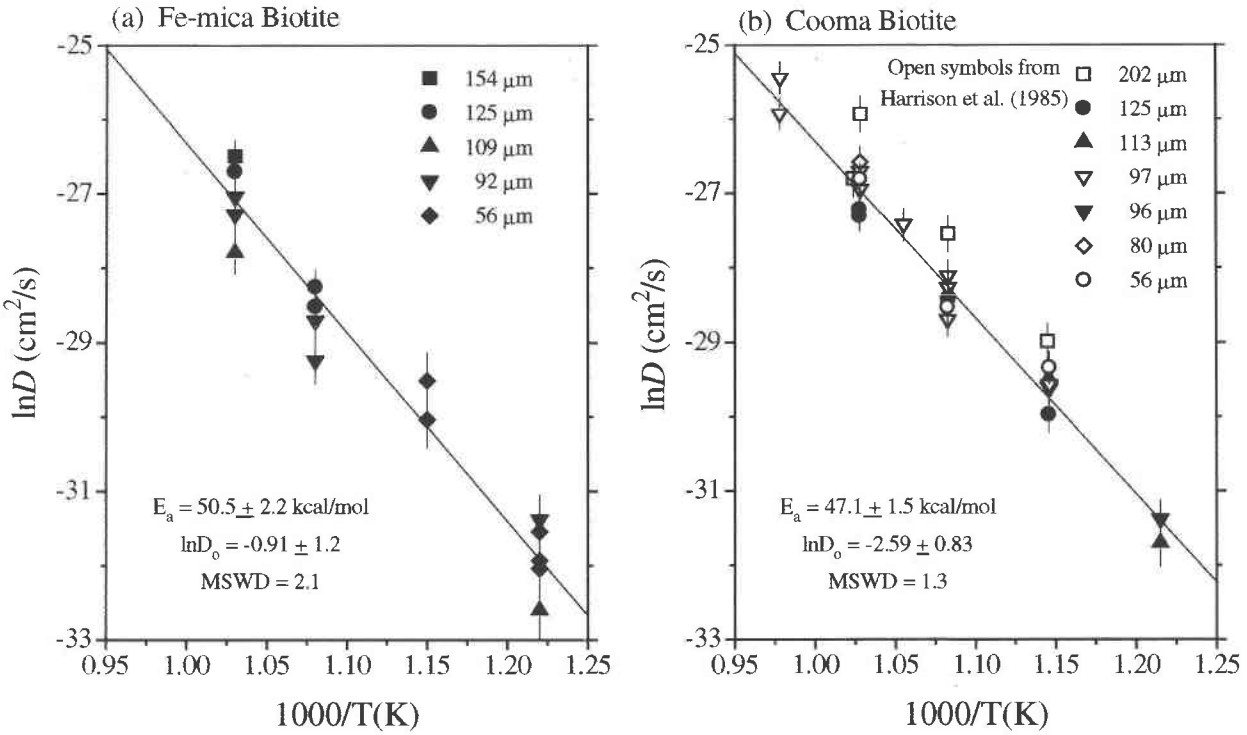

FIGURE 4. Arrhenius plots for Cooma biotite and Fe-mica (infinite-cylinder model). **(a)** Diffusion coefficients calculated for Fe-mica. **(b)** Results for Cooma biotite, including data from Harrison et al. (1985). Note that the values are nearly identical to those for Fe-mica biotite. Results obtained for Cooma biotite (solid symbols) in the present study agree with those of Harrison et al. (1985; open symbols) within the experimental uncertainty, except for the a = 202 μm size fraction. Analytical uncertainties are 1σ and reflect uncertainties in fractional loss and calculated grain radii. The reproducibility of diffusion coefficients at a given temperature is explained by experimental uncertainty at the 2σ level. Much of the variability is believed to result from minor recrystallization and the presence of grain fragments formed during initial pressurization that remained after ultrasonic cleaning and resizing.

indicated in Figure 5, the majority of the results agree with the infinite-cylinder solution within experimental uncertainty.

An alternative interpretation, advanced by Villa and Puxeddu (1994), of the mechanisms governing $^{40}Ar^*$ loss from biotite in hydrothermal experiments holds that $^{40}Ar^*$ is liberated primarily as a result of dissolution-reprecipitation reactions. These workers note that the dissolution rates (k_{diss}) indicated by Wood and Walther's (1983) Arrhenius-type relationship [3.5×10^{-12} to 1.2×10^{-11} mol biotite($cm^2 \cdot s$) over the temperature range 550–700 °C] predict substantial to complete dissolution of the biotite in hydrothermal experiments performed under conditions similar to those employed in the present study. The low solubility of biotite at 500–700 °C, 1000 bar conditions (Frantz et al. 1981) and the 4% by weight H_2O content of the charges require that nearly all dissolved biotite be precipitated as new grain growth. Preservation of original grain morphologies and lack of evidence for volumetrically significant new grain growth in the present experiments indicate that values of k_{diss} obtained from the Wood and Walther (1983) model are significantly overestimated for biotite under these conditions. For example, the minor textural changes noted for Fm-12 (Fig. 3), which was heated at 700 °C for 78 d, are grossly inconsistent with the 58% recrystallization that would be required to explain Ar loss by this mechanism. Moreover, the activation energy determined for $^{40}Ar^*$ retention in biotite grains examined in this study (47–51 kcal/mol) is significantly higher than the 13.3 kcal/mol activation enthalpy required by the Wood and Walther (1983) model. The apparent inability of the dissolution model to account for the experimental results may be explained by difficulties inherent in estimating effective surface area of grains and failure to adequately account for deviation from steady-state conditions caused by damaged grain surfaces (Helgeson et al. 1984; Kerrick et al. 1991). Values of k_{diss} for steady-state silicate hydrolysis, for example, have been found to differ by more than four orders of magnitude at constant temperature (Murphy and Helgeson 1989).

Incongruent dissolution of K represents an additional potential pitfall. Because fractional loss is calculated from changes in the $^{40}Ar^*/^{39}Ar$ ratio rather than from measured differences in $^{40}Ar^*$ concentrations, values of f are erroneous if the K content of mica is altered by incongruent dissolution during hydrothermal treatment (Hess et al.

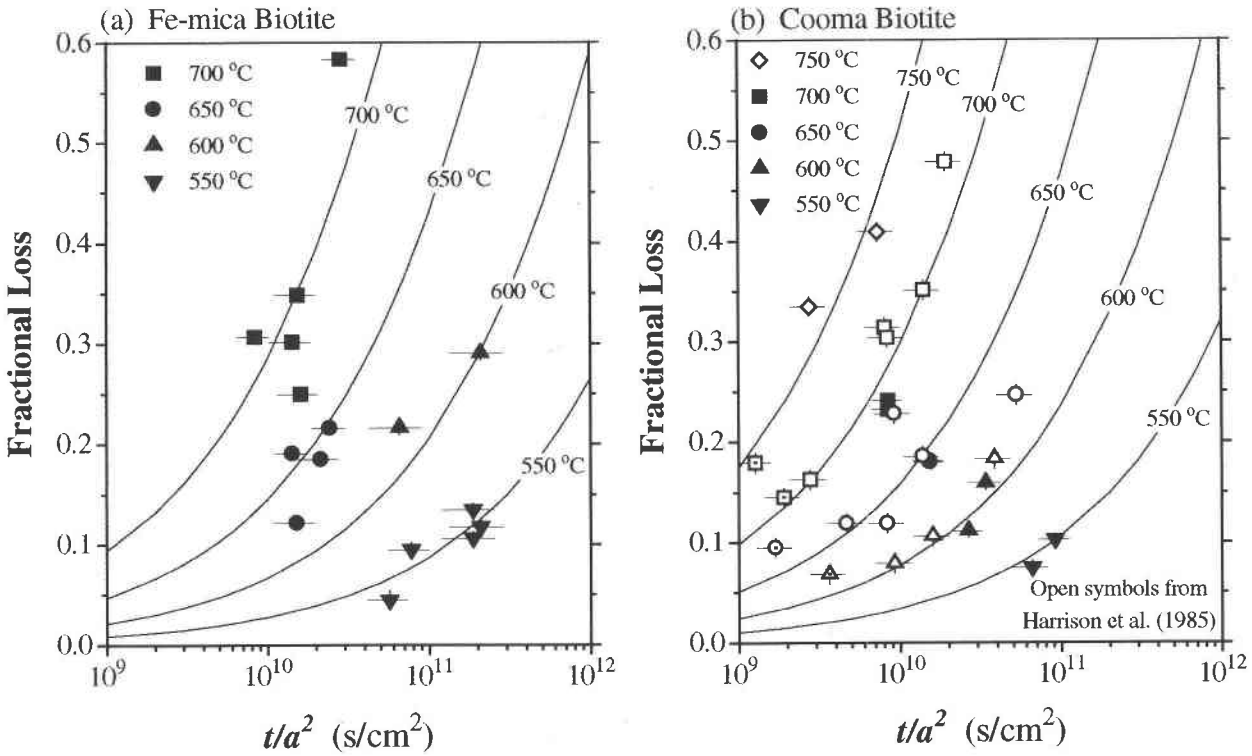

FIGURE 5. Plots of fractional loss (f) vs. t/a^2, where a and t represent the measured grain radius and heating duration, respectively. Error bars reflect propagation of uncertainties associated with a and the experimental uncertainty in f. Solid curves are calculated for the single-domain, infinite-cylinder model at the indicated temperatures. Results for Fe-mica biotite are indicated in **a** and those for Cooma biotite are shown in **b**. Open symbols represent results of Harrison et al. (1985). Open symbols with dots represent the $a = 0.0202$ cm size fraction. Note that experimental results for both Fe-mica and Cooma biotite define nearly two orders of magnitude variation in t/a^2 and generally fall within 1σ of the solution of the infinite-cylinder model. This relationship reveals compatibility of the results with the single-domain diffusion model.

1987). Although imprecise (±10%), equivalent percent K_2O can be calculated from the ^{39}Ar yields of both untreated and hydrothermally heated biotite (Table 4). Values obtained for untreated and treated Fe-mica biotite (9.1 ± 0.6 and 9.1 ± 0.9 $\%K_2O$, respectively) are identical and similar to the 8.8 ± 0.4 $\%K_2O$ value reported by Govindaradu (1979). Similarly, percent K_2O values obtained for Cooma biotite (9.6 ± 0.3 and 9.9 ± 0.4 for untreated and treated grains, respectively) agree well with the 9.8 $\%K_2O$ value reported by Tetley (1978). These results indicate that incongruent dissolution of K can be ruled out at the 10% level.

Uncertainty regarding the nature of $^{40}Ar^*$ concentration gradients developed in the hydrothermally treated mica prevents alternative diffusion mechanisms from being precluded. Use of natural biotite presents special problems in that both the diffusion geometry and the actual length scales of diffusion are not known with certainty. Moreover, extended defects and intergrown chlorite or similar phases in biotite may also significantly influence these parameters. Interestingly, laser-spot–profiling studies of naturally heated, millimeter-scale biotite and phlogopite (Phillips and Onstott 1988; Onstott et al. 1991; Phillips 1991; Kelley et al. 1994b) and other micas (e.g., Hodges et al. 1994) have reported $^{40}Ar^*$ loss profiles that appear inconsistent with those predicted for single-domain volume diffusion. Although some intragrain discontinuities are typically imaged, $^{40}Ar^*$ concentration gradients are predominately developed normal to grain boundaries over length scales typically corresponding to grain dimensions. Additionally, integrated ages tend to be somewhat younger than those predicted by single-domain intracrystalline diffusion. These observations have been cited as evidence for the existence of high-diffusivity pathways operating over length scales corresponding to grain dimensions (Onstott et al. 1991; Lee 1995). Unfortunately, similar detailed laser-spot–profiling of hydrothermally treated mica grains examined in the present study to determine concentration gradients was precluded by their small dimensions. Moreover, use of coarser materials is limited practically by the minimal amount of bulk $^{40}Ar^*$ loss (~1%) that can be induced during hydrothermal heating (≤700 °C) on laboratory time scales (e.g., Onstott et al. 1991).

An apparent discontinuous relationship between grain dimensions and apparent ^{40}Ar retentivity not anticipated

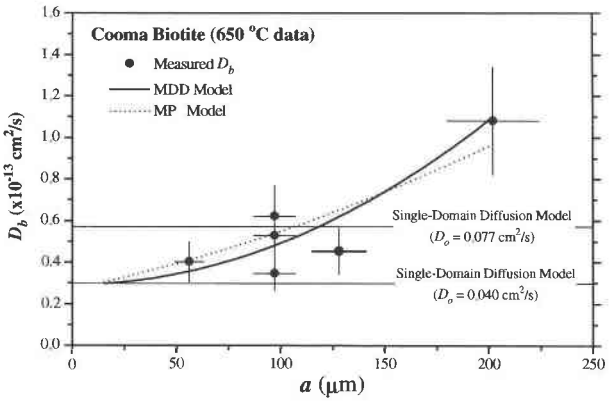

FIGURE 6. Measured or bulk diffusion coefficients (D_b) of Cooma biotite in 650 °C experiments of the present study and Harrison et al. (1985) plotted as a function of grain size (a). The horizontal lines represent two solutions for single-domain diffusion using an activation energy (E_a) of 47 kcal/mol and preexponential frequency factors (D_0) of 0.077 and 0.040 cm²/s, respectively. The dashed line represents a solution from the multipath (MP) model calculated by Lee [1995; see Table 2 and Fig. 4 of Lee (1995) for details]. The solid line represents a solution from the multiple diffusion domain (MDD) model with a domain distribution consisting of a single large domain accounting for 98.5% of the volume and smaller, a = 0.0015 cm domains totaling 1.5 vol%. In all instances the dimensions of the largest domain in the MDD model are negligibly smaller than actual grain dimensions. Both solutions provide an equally satisfactory fit to the observed data. The MDD solution indicates a preexponential frequency factor (D_0) of ~0.040 cm²/s and implies that the value of D_0 determined from regression of experimental data from all temperatures (0.077 cm²/s) was overestimated by a factor of two.

by single-domain intracrystalline diffusion models has been observed in hydrothermal experiments. For example, experiments by both Giletti (1974) and Harrison et al. (1985) indicated that Arrhenius results from relatively coarse-grained mica (a > 200 μm) were found to plot at systematically higher diffusivities than those calculated for finer grained mica (Fig. 4). Note that only grains <150 μm were used in the present study. Harrison et al. (1985) interpreted the enhanced diffusivity exhibited by the coarse mica to indicate the existence of an effective diffusion radius (a_{eff}) of ~150 μm. Similar discontinuous relationships between grain dimensions and apparent ^{40}Ar retentivity have also been observed in total fusion studies of biotite heated in nature (e.g., Wright et al. 1991).

Transport of $^{40}Ar^*$ along high-diffusivity pathways operating over length scales corresponding to grain dimensions during hydrothermal heating has been argued for by Onstott et al. (1991) and others. Lee (1995) presented calculations that demonstrate that increase in bulk diffusivity with grain radius can be explained as being a direct manifestation of high-diffusivity pathways in the multipath model (MP; Lee and Adama 1992). In the MP model, progressively more $^{40}Ar^*$ is able to diffuse out of the crystal along interconnected, high-diffusivity pathways as the overall grain dimensions increase (Fig. 6). We emphasize however, that the observed behavior can also be easily explained with the multiple diffusion domain model (MDD; Lovera et al. 1989; Lovera 1992). An argument typically employed against the possible existence of an effective diffusion radius for biotite is the failure to recognize compositional subdomains in $^{40}Ar/^{39}Ar$ laser-spot fusion studies (e.g., Phillips and Onstott 1988). However, the concept of an effective diffusion radius necessarily requires multiple diffusion domains that differ in dimension. In the MDD model, many domain distributions are capable of explaining the anomalously high diffusivities exhibited by the coarse-size fractions. These include distributions in which the largest domains are comparable in dimension to the observed grain size (Table 5).

TABLE 5. Calculation of effective radii of diffusion

a (cm)	ϕ	D/a^2 (1/s)	D_b (cm²/s)*	a_{eff} (cm)**
		Experimental†		
0.0202	1.0000	2.647 × 10⁻⁹	1.08 × 10⁻¹²	0.0147
		Distribution 1		
0.0150	0.4095	2.539 × 10⁻⁹		
0.0145	0.5905	2.722 × 10⁻⁹		
	bulk‡ D/a^2	2.647 × 10⁻⁹	1.08 × 10⁻¹²	0.0147
		Distribution 2		
0.0201	0.9852	1.414 × 10⁻⁹		
0.0026	0.0148	8.483 × 10⁻⁸		
	bulk‡ D/a^2	2.647 × 10⁻⁹	1.08 × 10⁻¹²	0.0147

Note: Calculations are based on E_a = 47000 cal/mol and D_0 = 0.077 cm²/s. A volume diffusivity of 5.71 × 10⁻¹³ cm²/s was determined from the Arrhenius equation [$D = D_0 \exp(-E_a/RT)$] at 650 °C. Volume fractions calculated assuming cylindrical shape with $a:l$ = 10:1, where l is one-half height of the cylinder. Individual domains sum to volume of a = 0.0202 cm cylinder ($a:l$ = 10:1).

* Bulk diffusivity calculated from bulk (D/a^2) value using a = 0.0202 cm.

** Effective radius (a_{eff}) for N diffusion domains calculated with $1/a_{eff}^2 = \Sigma_{i=1}^{N} f_i/a_i^2$.

† Results for experiment CB-0 in Table 2 of Harrison et al. (1985).

‡ Bulk D/a^2 calculated for N diffusion domains calculated with $D/a_{eff}^2 = \Sigma_{i=1}^{N} f_i D/a_i^2$.

To demonstrate, consider the specific example employed by Lee (1995; results of Harrison et al. 1985 reproduced in Table 5). In this experiment, the diffusivity calculated from the experimental results using a = 0.0202 cm was higher by a factor of about two than the values yielded by smaller grains. The value of a_{eff} required to reconcile the results in this instance is 0.0147 cm. Note that although the results can be modeled with a distribution of length scales comparable to a_{eff} (distribution 1 in Table 5), an equally plausible distribution consisting of a single large domain and a significantly smaller one also provides a satisfactory fit (distribution 2 in Table 5). In fact, many such distributions exist in which small domains not resolvable by $^{40}Ar/^{39}Ar$ laser-spot–profiling techniques increase bulk diffusivity. Given that typical spot sizes employed during $^{40}Ar/^{39}Ar$ laser-profiling studies are ~25 μm, a grain characterized by such a distribution would appear to have $^{40}Ar^*$ loss gradients controlled by grain boundaries and would yield a total gas

age lower than that anticipated from a single-domain diffusion model.

In the bulk-loss experiments, the Arrhenius parameters were determined following the assumption that a_{eff} corresponds to measured grain dimensions (a_{meas}). The value obtained for D_0 by regressing the experimentally determined bulk diffusivities represents an upper limit to the extent that a_{eff} is smaller than the measured than a_{meas}. This relationship is illustrated in Figure 6. Here, grains from each size fraction were considered to be characterized by a single large domain corresponding to 98.5% of the total volume of the grain and a smaller (a = 0.0015 μm) domain accounting for the remaining 1.5%. With D_0 equal to 0.040 cm^2/s instead of 0.077 cm^2/s, the fit to the experimental data is equally satisfactory as that provided by the multipath model, implying that the value for D_0 was overestimated by a factor of two. Note that although the existence of effective radii of diffusion is supported by apparent age–grain size relationships observed for biotite heated in nature (Wright et al. 1991), the existence of the smaller domains in the experimentally heated mica could represent an experimental artifact: Incomplete removal of broken grains formed as the experiments were initially pressurized.

Application to thermochronology

Single-domain, intracrystalline diffusion represents the simplest model available for Ar transport in biotite or other silicates that possess the predictive value required for thermochronology. Calculation of bulk closure temperatures from experimentally determined diffusion parameters is straightforward when a single-domain diffusion model is employed (e.g., Goodwin and Renne 1991; Hess et al. 1993). For example, bulk closure temperatures of 310 ± 40 and 330 ± 50 °C are calculated for Cooma biotite and Fe-mica biotite, respectively, using Dodson's (1973) solution of the diffusion equation, the experimentally determined Arrhenius parameters, and assuming a = 0.015 cm and 10 °C/Ma cooling. More complex $^{40}Ar^*$ retention properties in biotite indicated by $^{40}Ar/^{39}Ar$ laser-spot–profiling studies dictate the use of more general diffusion models such as MP or MDD that are capable of describing this behavior. Unfortunately these models introduce additional parameters that are unlikely to be constrained by $^{40}Ar/^{39}Ar$ data because of the instability of biotite during in vacuo incremental heating experiments.

As a first approximation, the MP and MDD models differ only in that interaction is permitted between intracrystalline domains and high-diffusivity pathways in the former but is precluded in the latter. This difference limits the predictive value of the MP model for thermochronology to a significantly greater extent than that of the MDD model. For example, interaction parameters must be constrained for every temperature to apply the MP model. Alternatively, all that is required to calculate a bulk closure temperature in the MDD model is a valid estimate of a_{eff}.

Values of a_{eff} can be estimated for a biotite of interest by comparing its diffusivity determined in a hydrothermal experiment with that calculated from appropriate Arrhenius parameters (Table 5). For example, Copeland et al. (1987) calculated a_{eff} = 0.034 cm for an intermediate biotite [$Fe_{tot}/(Fe_{tot} + Mg)$ = 0.49, a = 0.08 ± 0.02 cm] from the Quxu pluton, southern Tibet, from the 7.8% $^{40}Ar^*$ loss incurred in a single hydrothermal experiment (T = 710 °C, $\Delta t = 5.15 \times 10^5$ s, f = 0.078) and by assuming applicability of Arrhenius parameters from Harrison et al. (1985). Assuming 10 °C/Ma cooling, this corresponds to a closure temperature of 335 °C. Villa and Puxeddu (1994) performed similar experiments (T = 710 °C, $\Delta t = 5.11 \times 10^5$ s) with $a \approx 0.0065$ cm grains of intermediate [$Fe_{tot}/(Fe_{tot} + Mg)$ = 0.50] biotite from the Larderello geothermal field. Although values of a_{eff} calculated from these results agreed favorably with measured grain dimensions, Villa and Puxeddu (1994) concluded that $^{40}Ar^*$ loss incurred during hydrothermal heating resulted from dissolution processes and that bulk closure temperatures for biotite in nature were significantly higher than those indicated by experimentally determined diffusion parameters.

As discussed below, it appears that most intermediate biotite compositions (Fig. 1) have similar Arrhenius parameters. However, large uncertainties regarding appropriate Arrhenius parameters for nontypical biotite compositions indicate that caution should be applied in the estimation of values of a_{eff} for these materials in the manner described above. For example, Onstott et al. (1991) employed different extrapolations between Giletti's (1974) Arrhenius parameters for phlogopite and those for intermediate biotite compositions (Norwood 1974; Harrison et al. 1985) for Benson Mines phlogopite [$Fe_{tot}/(Fe_{tot} + Mg)$ = 0.21, a = 0.155 cm, f = 0.0133, T = 700 °C] and found that a_{eff} varied between 0.11 and 0.18 cm (note that the latter value is physically impossible).

Effect of biotite composition on Ar retentivity

The remarkable similarity of experimental results obtained for Fe-mica biotite and Cooma biotite casts serious doubt upon the view that Ar retentivity in biotite increases simply as a function of Fe content, as proposed by Norwood (1974) and Harrison et al. (1985). When the current experimental results are considered together with those of Hess et al. (1987) and Norwood (1974), it appears most probable that typical intermediate biotite compositions such as those depicted in Figure 1 possess broadly similar $^{40}Ar^*$ diffusion properties.

Within silicate structures, the diffusion energetics of a chemically inert substance such as Ar are likely to depend primarily upon potential energy changes incurred in the distortion of bonds of adjacent atoms during intracrystalline diffusion (Sardarov 1961). Note that crystalline defects and phase boundaries with intergrown phases such as chlorite also represent likely sites for Ar residence. However, although high-diffusivity pathways related to the occurrence of these features could significantly facil-

itate $^{40}Ar^*$ transport from biotite (Hess et al. 1987; Lo and Onstott 1989; Onstott et al. 1991; Lee 1995), the effects are unpredictable because of uncertainties regarding their volumetric significance and degree of interconnectivity. Because of its large size, radiogenic Ar confined within homogeneous mica is likely to be confined to vacant interlayer sites between the comparatively closer packed 2:1 layer units. This is demonstrated by the ionic porosity model, which predicts significantly higher diffusivities in the interlayer region relative to either the tetrahedral or octahedral sheets (Fortier and Giletti 1989).

Halogens substituted for OH groups may play a significant role in $^{40}Ar^*$ retentivity. Interlayer bonding forces in biotite are primarily due to electrostatic attraction between uncompensated charges on the 2:1 layer structures and the interlayer cations (Bailey 1984). In trioctahedral micas, the strength of the interlayer bond is appreciably weakened by the positioning of the OH group (Giese 1984). Because occupation of all three octahedral sites forces the OH group to be oriented essentially perpendicular to (001), the exposed proton is situated directly above K^+ in the interlayer cavity. K^+-H^+ repulsion reduces the interlayer attraction, increasing the basal spacing and destabilizing the interlayer cation (Giese 1984). This repulsion is progressively eliminated by substitution of F^- or Cl^- for the OH group with concomitant reduction in cell parameters (Noda and Ushiro 1964; Takeda and Morosin 1978). Calculations performed by Giese (1984) indicate that interlayer bonding energies increase by about 5 kcal/mol or 25% with substitution of F^- for OH^- in phlogopite. The higher F content of Fe-mica biotite could explain its slightly higher $^{40}Ar^*$ retentivity relative to Cooma biotite (Table 1). Note that because the maximum amount of Cl^- substitution for OH^- is small (generally <5–10%) relative to the amount of F^- that may be accommodated (up to 100%), F concentration plays the major role in influencing interlayer bonding in biotite (Munoz 1984). The apparent increase in $^{40}Ar^*$ diffusivity with increasing Mg/(Mg + Fe) could be linked to F content. The affinity of F for Mg-rich biotite has been well documented (Guidotti 1984; Speer 1984). The F-rich (66%) phlogopite examined by Giletti (1974) is significantly more retentive of $^{40}Ar^*$ than the intermediate biotite compositions investigated here.

Acknowledgments

We thank O.M. Lovera, C.E. Manning, M.T. Heizler, W.A. Dollase, and P.S. Dahl for helpful discussions. We are particularly grateful for assistance by R.J. Jones in electron microprobe measurements, SEM imaging, and determination of the cell parameters of the starting materials. We thank B.J. Giletti for supplying us with biotite samples studied by Norwood (1974) for electron microprobe analysis. M. Cosca and I. Villa are acknowledged for providing constructive reviews, which improved the manuscript.

References cited

Bailey, S.W. (1984) Crystal chemistry of the true micas. In Mineralogical Society of America Reviews in Mineralogy, 13, 13–60.

Brandt, S.B., Smirnov, V.N., Lapides, I.L., Volkova, N.V., and Kovalenko, V.I. (1967) Radiogenic argon as geochemical indicator of hydrothermal stability of some minerals. Geochemistry International, 4, 826–829.

Cebula, G.T., Kunk, M.J., Mehnert, H.H., Naeser, C.W., Obradovich, J.D., and Sutter, J.F. (1986) The Fish Canyon Tuff, a potential standard for the ^{40}Ar-^{39}Ar and fission-track dating methods (abs.). Terra Cognita, 6, 139.

Copeland, P., Harrison, T.M., Kidd, W.S.F., Ronghua X., and Yuquan, Z. (1987) Rapid early Miocene acceleration of uplift in the Gangdese belt, Xizang (southern Tibet), and its bearing on the accommodation mechanism of the India-Asia collision. Earth and Planetary Science Letters, 86, 240–252.

Crank, J. (1975) The mathematics of diffusion, 414 p. Oxford University Press, New York.

Dodson, M.H. (1973) Closure temperature in cooling geochronological and petrological systems. Contributions to Mineralogy and Petrology, 40, 259–279.

Foland, K.A. (1974) ^{40}Ar diffusion in homogeneous orthoclase and an interpretation of Ar diffusion in K-feldspar. Geochimica et Cosmochimica Acta, 38, 151–166.

Fortier, S.M., and Giletti, B.J. (1989) An empirical model for predicting diffusion coefficients in silicate minerals. Science, 245, 1481–1484.

Frantz, J.D., Popp, R.K., and Boctor, N.Z. (1981) Mineral-solution equilibria: V. Solubilities of rock forming minerals in supercritical fluids. Geochimica et Cosmochimica Acta, 45, 69–78.

Gaber, L.J., Foland, K.A., and Corbato, C.E. (1988) On the significance of argon release from biotite and amphibole during $^{40}Ar/^{39}Ar$ vacuum heating. Geochimica et Cosmochimica Acta, 52, 2457–2465.

Giese, R.F. (1984) Electrostatic energy models of micas. In Mineralogical Society of America Reviews in Mineralogy, 13, 105–144.

Giletti, B.J. (1974) Studies in diffusion: I. Argon in phlogopite mica. In A.W. Hofmann, B.J. Giletti, H.S. Yoder, and R.A. Yund, Eds., Geochemical transport and kinetics, p. 107–115. Carnegie Institute of Washington, publication 634.

Goodwin, L.B., and Renne, P.R. (1991) Effects of progressive mylonitization on Ar retention in biotites from the Santa Rosa mylonite zone, California, and thermochronologic implications. Contributions to Mineralogy and Petrology, 108, 283–297.

Govindaradu, K. (1979) Report (1968–1978) on two mica reference samples: Biotite Fe-mica and phlogopite mica-Mg. Geostandards Newsletter, 3, 3–24.

Grove, M., and Harrison, T.M. (1994) Argon loss from F-OH phlogopite. U.S. Geologic Survey Circular, 1107, 119.

Guidotti, C.V. (1984) Micas in metamorphic rocks. In Mineralogical Society of America Reviews in Mineralogy, 13, 357–468.

Hanson, G.N., and Gast, P.W. (1967) Kinetic studies in contact metamorphic zones. Geochimica et Cosmochimica Acta, 31, 1119–1153.

Hansen, G.N., Simmons, K.R., and Bence, A.E. (1975) $^{40}Ar/^{39}Ar$ age spectrum ages for biotite, hornblende, and muscovite in a contact metamorphic zone. Geochimica et Cosmochimica Acta, 39, 1269–1277.

Harrison, T.M., Duncan, I., and McDougall, I. (1985) Diffusion of ^{40}Ar in biotite: Temperature, pressure and compositional effects. Geochimica et Cosmochimica Acta, 49, 2461–2468.

Harrison, T.M., and Fitz Gerald, J.D. (1986) Exsolution in hornblende and its consequences for $^{40}Ar/^{39}Ar$ age spectra and closure temperature. Geochimica et Cosmochimica Acta, 50, 247–253.

Helgeson, H.C., Murphy, W.M., and Aagaard, R. (1984) Thermodynamics and kinetic constraints on reaction rates among minerals and aqueous solutions: II. Rate constants, effective surface area, and the hydrolysis of feldspar. Geochimica et Cosmochimica Acta, 48, 2405–2432.

Hess, J.C., Lippolt, H.J., and Wirth, R. (1987) Interpretation of $^{40}Ar/^{39}Ar$ spectra of biotites: Evidence from hydrothermal degassing experiments and TEM studies. Chemical Geology, 66, 137–149.

Hess, J.C., Lippolt, H.J., Gurbanov, A.G., and Michalski, I. (1993) The cooling history of the late Pliocene Eldzhurtinskiy granite (Caucasus, Russia) and the thermochronologic potential of grain size/age relationships. Earth and Planetary Science Letters, 117, 393–406.

Hodges, K.V., Hames, W.E., and Bowring, S.A. (1994) $^{40}Ar/^{39}Ar$ age gradients in micas from a high-temperature, low-pressure metamorphic terrane: Evidence for very slow cooling and implications for the interpretation of age spectra. Geology, 22, 55–58.

Huebner, J.S. (1971) Buffering techniques for hydrostatic systems at elevated pressures. In G.C. Ulmer, Ed., Research techniques for high pressure and high temperature, p. 123–178. Springer-Verlag, New York.

Kelley, S.P., Arnaud, N.O., Carroll, M.R., and Draper, D.S. (1994a) A UV laser ablation microprobe technique for argon isotope analysis. U.S. Geologic Survey Circular, 1107, 166.

Kelley, S.P., Reddy, S.M., and Maddock, R. (1994b) Laser-probe $^{40}Ar/^{39}Ar$ investigation of a pseudotachylite and its host rock from the outer Isles thrust, Scotland. Geology, 22, 443–446.

Kerrick, D.M., Lasaga, A.C., and Raeburn, S.P. (1991) Kinetic of heterogeneous reactions. In Mineralogical Society of America Reviews in Mineralogy, 26, 583–671.

Lee, J.K.W. (1995) Multipath diffusion in geochronology. Contributions to Mineralogy and Petrology, 120, 60–82.

Lee, J.K.W., and Adama, A.A. (1992) Multipath diffusion: A general numerical model. Computers and Geosciences, 18, 531–555.

Lo, C.H., and Onstott, T.C. (1989) ^{39}Ar recoil artifacts in chloritized biotite. Geochimica et Cosmochimica Acta, 53, 2697–2711.

Lovera, O.M. (1992) Computer programs to model $^{40}Ar/^{39}Ar$ diffusion data from multidomain samples. Computers and Geosciences, 18, 789–813.

Lovera, O.M., Richter, F.M., and Harrison, T.M. (1989) The $^{40}Ar/^{39}Ar$ thermochronometry for slowly cooled samples having a distribution of domain sizes. Journal of Geophysical Research, 94, 17917–17935.

McDougall, I., and Harrison, T.M. (1988) Geochronology and thermochronology by the $^{40}Ar/^{39}Ar$ method, 212 p. Oxford Monographs on Geology and Geophysics, Oxford University Press, New York.

Munoz, J.L. (1984) F-OH and Cl-OH exchange in micas with applications to hydrothermal ore deposits. In Mineralogical Society of America Reviews in Mineralogy, 13, 469–494.

Murphy, W.M., and Helgeson, H.C. (1989) Thermodynamic and kinetic constraints on reaction rates among minerals and aqueous solutions: IV. Retrieval of rate constants and activation parameters for the hydrolysis of pyroxene, wollasotonite, olivine, anadalusite, quartz, and nepheline. American Journal of Science, 289, 17–101.

Noda, T., and Ushiro, M. (1964) Hydrothermal synthesis of fluorine-hydroxyl-phlogopite: Part II. Relationship between the fluorine content, lattice constants, and the conditions of synthesis of fluorine-hydroxyl-phlogopite. Geochemistry International, 1, 96–104.

Norwood, C.B. (1974) Radiogenic argon diffusion in the biotite micas, 58 p. M.S. thesis, Brown University, Providence, Rhode Island.

Onstott, T.C., Phillips, D., and Pringle-Goodell, L. (1991) Laser microprobe measurement of chlorine and argon zonation in biotite. Chemical Geology, 90, 145–168.

Ozima, M., and Podosek, F.A. (1983) Noble gas geochemistry, 367 p. Cambridge University Press, Cambridge.

Phillips, D. (1991) Argon isotope and halogen chemistry of phlogopite from South African kimberlites: A combined step-heating, laser probe, electron microprobe and TEM study. Chemical Geology, 87, 71–98.

Phillips, D., and Onstott, T.C. (1988) Argon isotopic zoning in mantle phlogopite. Geology, 16, 542–546.

Reichenberg, D. (1953) Properties of ion-exchange resins in relation to their structure: III. Kinetics of exchange. American Chemical Society Journal, 75, 589–597.

Roubault, M., de La Roche, H., and Govindaraju, K. (1968) Report (1966–1968) on geochemical standards: Granites GR, GA, GH; basalt BR; ferriferous biotite mica-Fe; phlogopite mica-Mg. Sciences de la Terre, Tome XIII, n. 4, 379–404.

Rutherford, M.J. (1973) The phase relations of aluminous iron biotites in the system $KAlSi_3O_8$-$KAlSiO_4$-Al_2O_3-Fe-O-H. Journal of Petrology, 14, 159–180.

Sanz, J., Gonzalez-Carreno, T., and Gancedo, R. (1983) On dehydroxylation mechanisms of a biotite in vacuo and in oxygen. Physics and Chemistry of Minerals, 9, 14–18.

Sardarov, S.S. (1961) Bond energy and retention of radiogenic argon in micas. Geochemistry International, 1, 33–44.

Speer, J.A. (1984) Micas in igenous rocks. In Mineralogical Society of America Reviews in Mineralogy, 13, 299–356.

Takeda, H., and Morosin, B. (1978) Comparison of observed and predicted structural parameters of mica at high temperature. Acta Crystallographica, B31, 2444–2452.

Tetley, N.W. (1978) Geochronology by the $^{40}Ar/^{39}Ar$ technique using HIFAR reactor, 287 p. Ph.D. thesis, Australian National University, Canberra, Australia.

Vedder, W., and Wilkins, R.W.T. (1969) Dehydroxylation and rehydroxylation, oxidation and reduction of micas. American Mineralogist, 54, 482–509.

Vernon, R.H. (1988) Sequential growth of andalusite and cordierite porphyroblasts, Cooma Complex, Australia: Microstructural evidence of a prograde reaction. Journal of Metamorphic Geology, 6, 255–269.

Villa, I.M., and Puxeddu, M. (1994) Geochronology of the Larderello geothermal field: New data and the "closure temperature" issue. Contributions to Mineralogy and Petrology, 115, 415–426.

Westcott, M.R. (1966) Loss of argon from biotite in a thermal metamorphism. Nature, 210, 83–84.

Wones, D.R., and Eugster, H.P. (1965) Stability of biotite: Experiment, theory, and application. American Mineralogist, 50, 1228–1272.

Wood, B.J., and Walther, J.V. (1983) Rates of hydrothermal reactions. Science, 222, 554–555.

Wright, N., Layer, P.W., and York, D. (1991) New insights into thermal history from single grain $^{40}Ar/^{39}Ar$ analysis of biotite. Earth and Planetary Science Letters, 104, 70–79.

MANUSCRIPT RECEIVED MARCH 9, 1995
MANUSCRIPT ACCEPTED MARCH 12, 1996

APPENDIX TABLE 1. Compositions of the biotite of Norwood (1974)

	Std-5	Std-6	Std-8
Si	2.77	2.80	2.79
$^{[4]}Al$	1.23	1.20	1.21
$^{[6]}Al$	0.19	0.28	0.12
Ti	0.16	0.12	0.18
Cr	0.00	0.00	0.00
Fe	1.11	1.29	1.08
Mn	0.02	0.02	0.02
Mg	1.35	1.11	1.33
K	0.94	0.96	0.95
Na	0.02	0.00	0.02
Total Cations	7.78	7.80	7.70

Note: Results of electron microprobe analysis performed at UCLA with materials supplied by B.J. Giletti. These compositions differ appreciably from those reported by Norwood (1974).